

Thermalization and free decay in surface quasigeostrophic flows

Tomas Teitelbaum¹ and Pablo D. Mininni^{1,2}

¹*Departamento de Física, Facultad de Ciencias Exactas y Naturales, Universidad de Buenos Aires and IFIBA, CONICET, Ciudad Universitaria, 1428 Buenos Aires, Argentina*

²*NCAR, PO Box 3000, Boulder, Colorado 80307-3000, USA*

(Received 8 October 2011; revised manuscript received 21 May 2012; published 30 July 2012)

We derive statistical equilibrium solutions of the truncated inviscid surface quasigeostrophic (SQG) equations, and verify the validity of these solutions at late times in numerical simulations. The results indicate the pseudoenstrophy thermalizes while the pseudoenergy can condense at the gravest modes, in agreement with previous indications of a direct cascade of pseudoenstrophy and an inverse cascade of pseudoenergy in forced-dissipative SQG systems. At early times, the truncated inviscid SQG simulations show a behavior reminiscent of forced-dissipative SQG turbulence, and we identify spectral scaling laws for the pseudoenergy and pseudoenstrophy spectra. More importantly, a comparison between viscous and inviscid simulations allows us to identify free-decay laws for the pseudoenstrophy in SQG turbulence at very large Reynolds number.

DOI: [10.1103/PhysRevE.86.016323](https://doi.org/10.1103/PhysRevE.86.016323)

PACS number(s): 47.27.ek, 47.27.eb, 92.10.Lq, 47.27.Gs

I. INTRODUCTION

Classical Gibbs ensemble methods have been extensively applied to Galerkin representation of turbulent systems, and many examples can be found in the literature. The first studies of the statistical mechanics of discrete distributions of vortices in a two-dimensional (2D) flow using a Hamiltonian formalism can be found in Ref. [1]. Later, it was shown [2] that Gibbsian statistical mechanics can be applied to Galerkin truncations of the hydrodynamic and magnetohydrodynamic (MHD) equations. This allowed many studies of continuous vorticity distribution in truncated 2D inviscid flows [3–6], where absolute equilibrium spectra for the quadratic conserved quantities of the system were derived. Following Ref. [3], in Ref. [7] the absolute inviscid equilibrium ensemble for three-dimensional (3D) Euler flows was considered. Later, 3D inviscid MHD equilibrium solutions were investigated in Ref. [8], and recently the approach was extended to Hall-MHD in Ref. [9]. Other problems studied in this framework include geophysical flows [10], fast rotating flows [11,12], and formulations of one- and two-layer quasigeostrophic models [13]. In general, classical Gibbs ensemble methods can be applied to systems with quadratic conserved quantities that satisfy the Liouville theorem, which implies the incompressibility of the flow in phase space (e.g., the space of complex Fourier modes).

In the absolute equilibrium, fields have Gaussian statistics and the quadratic conserved quantities of the system have associated temperatures that can be positive or negative. In the former case, the quantity is said to “thermalize,” and the quantity in the equilibrium is equally distributed among all modes in the system. In the latter case the quantity “condenses” and is accumulated at the gravest modes. However, forced-dissipative turbulent systems are far from equilibrium, as the effect of viscosity prevents relaxation towards a true equilibrium state, giving rise to solutions with nonzero flux (cascades) and making direct comparison with equilibrium solutions inadequate. In spite of this, Gibbs ensemble methods proved useful to predict the direction of the cascades in many forced-dissipative systems, depending on whether the quantity of interest thermalized or condensed in the associated truncated inviscid system (see, e.g., [4,7,10,14], although note not all

inverse cascades in forced-dissipative systems are associated with condensates in the statistical equilibrium of the equivalent truncated ideal system [11,12]).

The recent finding of transients and quasistable states in truncated inviscid flows, in which nonthermalized modes behave as in the viscous case (see, e.g., [15–18]), has renewed interest in classical Gibbs ensembles, indicating more information than just the direction of the cascades can be extracted from these systems. In particular, it was found that at early times and as the system evolves towards equilibrium, a comparison between the inviscid system and a viscous turbulent flow can be achieved by considering in the inviscid system the net effect of the modes that have already thermalized as an effective viscosity acting on the nonthermalized modes [16,18]. This viscouslike dynamics was reported in many systems, including the 3D truncated Euler equation [15,16,18], 3D truncated rotating flows [12], 2D truncated MHD [19], and turbulent Bose-Einstein condensates using the truncated Gross-Pitaevskii equations [20]. In this latter case, the truncated equations allowed the study of thermalization of Bose-Einstein condensates at finite temperature.

Classical Gibbs ensembles and quasistable states were also used to study the behavior of atmospheric models (see, e.g., [21]), as the need to study atmospheric and oceanic flow dynamics has led to a variety of approximate models derived from the 3D Navier-Stokes equation for stratified and rotating flows (see, e.g., [22–24]). In the often used geostrophic approximation, the vertical component of the velocity field is assumed zero ($u_z = 0$), and hydrostatic balance is solved in that direction while a linear balance between the Coriolis force and the pressure gradient is solved on the horizontal plane. Another family of models is given by the so-called quasigeostrophic (QG) models, which are a first-order departure from the linear geostrophic balance on the horizontal plane. That truncated QG systems satisfy the Liouville theorem, thus allowing the use of Gibbs ensemble methods, can be seen, for example, in Ref. [21].

A particular case of the QG models is the surface quasigeostrophic (SQG) approximation [25–30], which describes rotating stratified flows with constant potential vorticity. In this model, the vertical gradient of the stream function ψ matches

a scalar field q (the density field ρ or the potential temperature T) at a flat surface $z = 0$. The scalar field is identified with the horizontal Laplacian $q = (-\Delta)^{1/2}\psi$, and the equation for the advection of this scalar by the incompressible surface flow $\mathbf{u} = \hat{z} \times \nabla\psi = (-\partial_y\psi, \partial_x\psi, 0)$ is solved. Contrary to 3D QG turbulence whose dynamics is driven by large-scale interior potential vorticity gradients, SQG flows are entirely driven by density or potential temperature variations at the surface. Recently, this system has been used to study the dynamics of the upper troposphere [31–33], and of the upper oceanic layers with relative accuracy down to 500 meters [34–36]. Turbulence in forced-dissipative SQG systems (including direction of cascades and scaling laws) has also been studied in numerical simulations [25,28,30].

Besides potential applications in ocean and atmospheric dynamics, the SQG equations have interest from the mathematical and physical points of view. Although the SQG equations are 2D in nature, their dynamics share similarities with the 3D Euler equations, and whether a singularity in the gradients of the scalar field develops at finite time from smooth initial conditions has been the focus of many mathematical and numerical studies [37–40].

In mathematics, attention is focused on the problem,

$$\partial_t q + \mathbf{u} \cdot \nabla q + \nu(-\Delta)^\mu q = 0. \quad (1)$$

The case $\mu = (\frac{1}{2}, 1]$, $\nu \geq 0$ is considered, with initial smooth data for $q(\mathbf{x})$ in R^2 . Many studies provide strict upper bounds to the long-term evolution of Lebesgue L^p and Sobolev norms of q and ∇q for weak solutions of Eq. (1), as some powers of time [38,40]. In particular, the results for the L^2 norm of q (the so-called pseudoenstrophy) is relevant for this work and will be discussed later.

Although there is no clear-cut answer in the most general case, a singularity has been ruled out for the case in which isolevels of the scalar contain a hyperbolic saddle [41]. Numerically it was also shown that initial conditions whose isolevels contain a hyperbolic saddle develop fronts faster than other known initial conditions.

In the same context, a numerical study of the growth of the gradient of the scalar field, with a comparison between the dynamics of the inviscid ($\nu = 0$) and viscous ($\nu > 0$) SQG equations, was carried in Ref. [42]. In this work one particular initial condition was considered, with $\mu = 1$ (the same value we use in the present work). The observed power spectrum of the scalar field disagrees with the turbulent one derived in Ref. [25], where the hypothesis of a direct enstrophy cascade and a finite dissipation rate in the inviscid limit is used. Indeed, in Ref. [42] the total dissipation rate of the pseudoenstrophy seems to vanish in the limit of infinite Reynolds number. For the initial condition and dissipation mechanism considered, this result suggests that the inviscid solution remains regular for all time.

More recently, cascades in the SQG equations have also received attention from the physical point of view, as it was found that large scales in SQG flows have conformal invariant properties [43].

In this paper we investigate the classical Gibbs ensemble solution of the truncated inviscid SQG equations, and compare these solutions and their viscouslike transient with

solutions of the dissipative SQG equations. In particular, we derive solutions for the pseudoenergy and pseudoenstrophy equilibrium spectrum, verify numerically the convergence of the truncated SQG solutions to the statistical equilibrium solutions, and compare inviscid and viscous numerical results. In the simulations, we consider four different smooth initial conditions including the ones used in Refs. [37,41,42], and a dissipation mechanism given by $\mu = 1$.

The statistical equilibrium solution indicates the pseudoenstrophy thermalizes while the pseudoenergy condenses in SQG, in agreement with previous numerical results where a direct cascade of pseudoenstrophy and an inverse cascade of pseudoenergy were reported [25,44]. In the viscouslike transient, we observe the development of inertial ranges with $\sim k^{-5/3}$ scaling for the spectrum of the pseudoenstrophy, unlike previous inviscid simulations where steeper power laws were observed [42] (the causes of this difference are explained). Finally, we present an analogy between the nonthermalized fraction of the pseudoenergy and pseudoenstrophy in the inviscid truncated runs, and the free decay of the pseudoenergy and pseudoenstrophy in the viscous SQG equations at very large Reynolds numbers. The analogy allows us to identify possible asymptotic behavior for very large Reynolds numbers.

The paper is organized as follows. In Sec. II we introduce the SQG equations and derive the statistical equilibrium solutions using the canonical distribution function formalism. In Sec. III we present a set of numerical simulations of the truncated inviscid SQG equations. We first compare them with the theoretical equilibrium solutions, and we then introduce a viscous SQG system comparing the time evolution of viscous and inviscid simulations. Finally, we present our conclusions in Sec. IV.

II. SQG AND THE GIBBS ENSEMBLE

The system considered in this paper is an incompressible 2D SQG flow. Its equations are usually presented in the literature as part of a family of equations governing the advection of a scalar [25]:

$$q = (-\Delta)^{\alpha/2}\psi. \quad (2)$$

This family includes the SQG equations ($\alpha = 1$, which is the case in the present study) [26,45], the vorticity equation in an Euler flow ($\alpha = 2$), and the equation of motion for a shallow flow in a rotating domain driven by uniform internal heating ($\alpha = 3$) [27]. The case $\alpha = -2$ corresponds to a shallow-water QG equation in the limit of large length scales compared to the deformation scale (see [46]).

The flow in these models is described by a stream function ψ , and governed by the so-called α -turbulence equations which, in their inviscid unforced version, are usually written in the general form:

$$\partial_t q + J(\psi, q) = 0, \quad (3)$$

where J is the Poisson bracket,

$$J(A, B) = \partial_x A \partial_y B - \partial_x B \partial_y A. \quad (4)$$

For SQG, Eq. (2) in Fourier space reduces to $\hat{q}(\mathbf{k}) = |\mathbf{k}|\hat{\psi}(\mathbf{k})$, and Eq. (3) reads

$$\partial_t \hat{\psi} = \frac{1}{|\mathbf{k}|} (\widehat{\partial_x q \partial_y \psi} - \widehat{\partial_x \psi \partial_y q}), \quad (5)$$

where the hats denote Fourier transformed. Inviscid SQG dynamics possesses two quadratic conserved quantities, analogous to the energy and enstrophy in 2D Euler flows, which are defined, respectively, as

$$E = -\frac{1}{A} \int q \psi \, dx dy, \quad (6)$$

and

$$G = \frac{1}{A} \int q^2 \, dx dy, \quad (7)$$

with A the total area of the integration domain. We will refer to these magnitudes as the pseudoenergy and pseudoenstrophy, respectively. Note that sometimes these quantities are defined with a factor 1/2 in front, in analogy with the energy and enstrophy in the 2D Euler equations (see, e.g., [45]). For the sake of simplicity, in the following we use the convention followed in Refs. [25,26] and drop those factors.

Note in the forced-dissipative case, Kolmogorov-Batchelor-Kraichnan phenomenology predicts two inertial ranges for these quantities [25]: an inverse cascade of pseudoenergy with spectra $E(k) \sim k^{-2}$ and $G(k) \sim k^{-1}$, and a direct cascade of pseudoenstrophy with spectra $E(k) \sim k^{-8/3}$ and $G(k) \sim k^{-5/3}$. We will consider this case in Sec. III.

Writing $k = |\mathbf{k}|$, the pseudoenergy and pseudoenstrophy of each Fourier mode \mathbf{k} are easily related by

$$G(\mathbf{k}) = kE(\mathbf{k}) = |\hat{\mathbf{u}}(\mathbf{k})|^2. \quad (8)$$

Since $\hat{u}_x(\mathbf{k}) = -ik_y \hat{\psi}(\mathbf{k})$, $\hat{u}_y(\mathbf{k}) = ik_x \hat{\psi}(\mathbf{k})$, and the relation between the pseudoenergy in each mode and the stream function is

$$|\hat{\mathbf{u}}|^2 = (k_x^2 + k_y^2) |\hat{\psi}|^2 = k^2 |\hat{\psi}|^2, \quad (9)$$

the pseudoenergy and pseudoenstrophy can then be written in Fourier space as follows:

$$E = \sum_{\mathbf{k}/k \in N'} k |\hat{\psi}(\mathbf{k})|^2, \quad (10)$$

$$G = \sum_{\mathbf{k}/k \in N'} k^2 |\hat{\psi}(\mathbf{k})|^2, \quad (11)$$

where $N' = \{1, \dots, N/2\}$ runs over all degrees of freedom of the system. Note that in Eqs. (10) and (11) we already truncated the system up to a finite number of modes.

From these relations we can derive the statistical equilibrium solutions for the inviscid truncated SQG system. The generalized Gibbs canonical distribution is

$$P = \frac{1}{Z} e^{-(\beta E + \gamma G)}, \quad (12)$$

where

$$Z = \int_{\text{phase space}} e^{-(\beta E + \gamma G)} d\xi \quad (13)$$

is the partition function and $d\xi = \prod_{\mathbf{k}} d\mathbf{u}_1(\mathbf{k}) d\mathbf{u}_2(\mathbf{k})$; \mathbf{u}_1 and \mathbf{u}_2 are defined such that $\hat{\mathbf{u}}(\mathbf{k}) = \mathbf{u}_1(\mathbf{k}) + i\mathbf{u}_2(\mathbf{k})$ and are

constrained by the incompressibility condition $\nabla \cdot \mathbf{u} = 0$ (or $\mathbf{k} \cdot \hat{\mathbf{u}} = 0$ in Fourier space) by

$$k_x \hat{u}_{1x} + k_y \hat{u}_{1y} = 0, \quad (14)$$

$$k_x \hat{u}_{2x} + k_y \hat{u}_{2y} = 0. \quad (15)$$

From Eqs. (9)–(11),

$$E = \sum_{\mathbf{k}/k \in N'} \frac{|\hat{\mathbf{u}}(\mathbf{k})|^2}{k}, \quad (16)$$

$$G = \sum_{\mathbf{k}/k \in N'} |\hat{\mathbf{u}}(\mathbf{k})|^2, \quad (17)$$

and the partition function results

$$\begin{aligned} Z &= \int e^{-\beta \sum \frac{|\hat{\mathbf{u}}(\mathbf{k})|^2}{k} - \gamma \sum |\hat{\mathbf{u}}(\mathbf{k})|^2} \prod_{\mathbf{k}/k \in N'} d\mathbf{u}_1(\mathbf{k}) d\mathbf{u}_2(\mathbf{k}) \\ &= \prod_{\mathbf{k}/k \in N'} 2\pi \int e^{-|\mathbf{u}_1(\mathbf{k})|^2 (\frac{\beta}{k} + \gamma)} |\mathbf{u}_1(\mathbf{k})| d\mathbf{u}_1(\mathbf{k}) \\ &\quad \times 2\pi \int e^{-|\mathbf{u}_2(\mathbf{k})|^2 (\frac{\beta}{k} + \gamma)} |\mathbf{u}_2(\mathbf{k})| d\mathbf{u}_2(\mathbf{k}). \end{aligned} \quad (18)$$

Note we used isotropy of the velocities \mathbf{u}_1 and \mathbf{u}_2 to convert the first integral in the entire phase space into two one-dimensional integrals with respect to the absolute values $u_1 = |\mathbf{u}_1|$ and $u_2 = |\mathbf{u}_2|$, respectively.

Using

$$\int_0^\infty e^{-x^2 (\frac{\beta}{k} + \gamma)} x dx = \frac{k}{2(\gamma k + \beta)}, \quad (19)$$

which holds provided $\text{Re}(\gamma + \beta/k) > 0$, the partition function results

$$Z = \prod_{\mathbf{k}/k \in N'} \left(\frac{\pi k}{\gamma k + \beta} \right)^2 = \prod_{\mathbf{k}/k \in N'} Z_{\mathbf{k}}. \quad (20)$$

The most probable probability density function can be obtained by other methods. A Lagrange multiplier method can be used (see Ref. [21]). Another elegant way is to use properties of n -dimensional normal distributions (see, e.g., [9]). All these methods yield the same result.

From the partition function we can derive the mean modal intensity spectra of pseudoenergy and pseudoenstrophy:

$$E(\mathbf{k}) = -\frac{\partial \ln Z_{\mathbf{k}}}{\partial \beta} = \frac{2}{\gamma k + \beta}, \quad (21)$$

$$G(\mathbf{k}) = -\frac{\partial \ln Z_{\mathbf{k}}}{\partial \gamma} = \frac{2k}{\gamma k + \beta}. \quad (22)$$

These spectra give the pseudoenergy and pseudoenstrophy in each mode \mathbf{k} , and are functions of its modulus only. The usual isotropic spectrum is obtained by integrating Eqs. (21) and (22), resulting, for example, in $E(k) = \pi k E(\mathbf{k})$ [5] provided the modes are dense enough over the entire spectrum. We then finally get the expressions for the isotropic spectra of pseudoenergy and pseudoenstrophy,

$$E(k) = \int E(\mathbf{k}) k d\varphi = \pi k E(\mathbf{k}) = \frac{2\pi k}{\gamma k + \beta}, \quad (23)$$

$$G(k) = \int G(\mathbf{k}) k d\varphi = \pi k G(\mathbf{k}) = \frac{2\pi k^2}{\gamma k + \beta}. \quad (24)$$

The pseudoenergy and pseudoenstrophy are quadratic magnitudes and therefore Eqs. (23) and (24) must be positive.

The relation $\gamma k > -\beta$ must apply to every value of k , and as the case $k = 1$ is the more restrictive, we simply need the system to satisfy the condition,

$$\gamma > -\beta. \quad (25)$$

This condition is enough for integral (19) to converge. Furthermore, asking the total pseudoenergy and pseudoenstrophy to be positive, it is obtained that $\gamma > 0$ and that the pseudoenstrophy thermalizes.

A truncated inviscid SQG system is expected to reach at large times the absolute equilibrium solutions (23) and (24). The values of γ and β are uniquely determined by the total amount of pseudoenergy and pseudoenstrophy contained in the initial conditions, and can be calculated solving the system of equations:

$$E(t=0) = \sum_k \frac{2\pi k}{\gamma k + \beta}, \quad (26)$$

$$G(t=0) = \sum_k \frac{2\pi k^2}{\gamma k + \beta}. \quad (27)$$

Note these equations can be easily converted to two polynomial equations with two unknowns (γ and β). The number of terms on the right-hand side of Eqs. (26) and (27) depend on the maximum wave number preserved after the truncation (and therefore, in numerical simulations, on the linear resolution N). As $E(t=0)$ and $G(t=0)$ are known, the system can be easily solved numerically. For the resolutions used in the next section, the values obtained for (γ, β) are as follows: (346.23, -342.60) for $N = 32$, (1344.79, -1341.39) for $N = 64$, (5044.05, -5040.75) for $N = 128$, (19504.20, -19500.90) for $N = 256$, (77579.35, -77576.13) for $N = 512$, and (311246.27, -311243.06) for $N = 1024$.

III. NUMERICAL RESULTS

In this section we present numerical simulations of the SQG equations. We first compare the inviscid spectra at late times stemming from the simulations with the results derived above. Then, we study the transition from the initial condition towards the equilibrium spectrum in simulations at larger spatial resolution, and compare the behavior of the nonthermalized fraction of pseudoenergy and pseudoenstrophy in the inviscid runs with the pseudoenergy and pseudoenstrophy in viscous runs.

A. Inviscid truncated runs

To solve numerically Eq. (5) in a 2D periodic domain of length 2π , we use a parallel pseudospectral code [47,48]. Second-order Runge-Kutta is used to evolve in time, and nonlinear terms are computed with the 2/3 rule for dealiasing, so that the Fourier space is truncated at the maximum wave number $k_{\max} = N/3$, with N the linear resolution. Under these conditions, pseudospectral methods are known to be equivalent to Galerkin spectral methods [49], and all quadratic invariants of the original equations are conserved in the truncated Fourier space. As an example, in simulations of the inviscid SQG equations with resolution of 512^2 grid points and a time step of $\Delta t = 2 \times 10^{-4}$, the pseudoenergy was conserved up to the fourth digit after 500 turnover times.

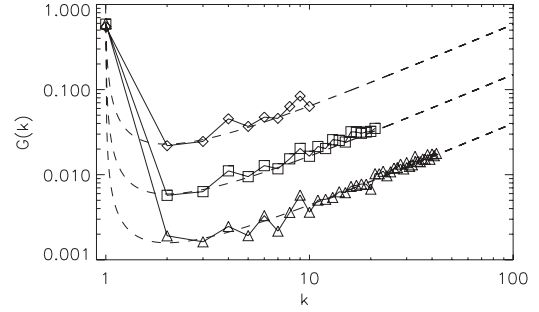


FIG. 1. Isotropic pseudoenstrophy spectra for runs with $N = 32$ (diamonds), 64 (squares), and 128 (triangles) at $t = 20, 1000$, and 24 000, respectively. The Gibbs ensemble prediction (24) for each run is shown in dashed lines. The values of (γ, β) obtained from solving Eqs. (26) and (27) for the initial pseudoenergy and pseudoenstrophy of the runs are (346.23, -342.60) for $N = 32$, (1344.79, -1341.39) for $N = 64$, and (5044.05, -5040.75) for $N = 128$. Theoretical and numerical results are in good agreement for all wave numbers.

Spatial resolutions ranged from 32^2 to 1024^2 grid points. The initial condition for all runs is a superposition of Fourier modes with random phases, with a pseudoenergy spectrum $E(k) \sim k^{-2}$ for $1 \leq k \leq 4$, and zero otherwise. All simulations behave in a similar fashion, showing a progressive thermalization of modes with higher wave number and reaching equilibrium for long times; however, simulations at larger resolution take longer time to reach equilibrium at all scales. Once the system reaches equilibrium, its spectrum should be compatible with solutions (23) and (24). To compare simulation results with the theoretical predictions, γ and β were determined solving the set of Eqs. (26) and (27) for each spatial resolution separately, as explained in the previous section.

Numerical results for the isotropic pseudoenstrophy spectrum once the equilibrium was reached are shown in Fig. 1, with different symbols for the numerical data, and with dashed lines for the theoretical predictions. Numerical spectra are in good agreement with the theory at all wave numbers, and the spectrum shows a peak at $k = 1$ (associated with the condensation of pseudoenergy at the gravest modes), and a $\sim k$ scaling (associated with the thermalization of pseudoenstrophy) for larger wave numbers. However, note that as the resolution is increased, the time to reach the equilibrium increases.

Results for higher resolutions (from 256^2 to 1024^2 grid points) at $t = 200$ together with their theoretical predictions are shown separately in Fig. 2. For higher resolutions, the thermalization process is slower and convergence of lower wave-number modes to the statistical equilibrium solution takes progressively longer times. Nevertheless, numerical and theoretical results agree well for intermediate to high wave numbers.

The slowdown of the thermalization as resolution is increased can also be seen in Fig. 3, that shows the time t_* for the system to have 50% of its pseudoenstrophy thermalized. Note this thermalization takes place predominantly at large wave numbers, and to reach the equilibrium at lower wave numbers takes substantially longer times.

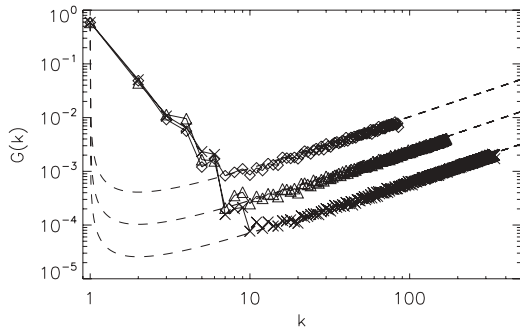


FIG. 2. Isotropic pseudoenstrophy spectra at $t = 200$ for runs with $N = 256$ (diamonds), 512 (triangles), and 1024 (crosses). The Gibbs ensemble prediction (24) is shown in dashed lines. The values of (γ, β) obtained from solving Eqs. (26) and (27) for the initial pseudoenergy and pseudoenstrophy of the runs are $(19504.20, -19500.90)$ for $N = 256$, $(77579.35, -77576.13)$ for $N = 512$, and $(311246.27, -311243.06)$ for $N = 1024$. As the resolution increases, it takes longer times for the equilibrium at large scales to be reached, while thermalization at large wave numbers is achieved fast.

Simulations at lower resolution provide as a result a faster way to verify the validity of the Gibbs ensemble prediction. However, to study the viscouslike transient that develops as the system evolves towards equilibrium, the runs with larger resolutions will allow us better identification of scaling laws and comparison with viscous runs. We therefore focus in the following on the 1024^2 run. Figures 4 and 5 show the time evolution of the pseudoenergy and pseudoenstrophy spectra in this run. At early times both spectra develop a viscouslike inertial range, with slopes compatible with Kolmogorov-Batchelor-Kraichnan phenomenology [25]. A power law $\sim k^{-5/3}$ can be identified in the pseudoenstrophy, and $\sim k^{-8/3}$ in the pseudoenergy spectrum. As time evolves, the pseudoenstrophy shows a progressive thermalization starting from the largest wave numbers, and the viscouslike inertial range becomes narrower as the $G(k) \sim k$ thermalized spectrum broadens. We will take the minimum of the pseudoenstrophy spectrum, at $k = k_{th}$, as the delimiting wave number between these two subranges. The flat pseudoenergy spectrum for $k > k_{th}$, and its peak at $k = 1$, evidences a condensation of this quantity at low k rather than a thermalization at high wave numbers.

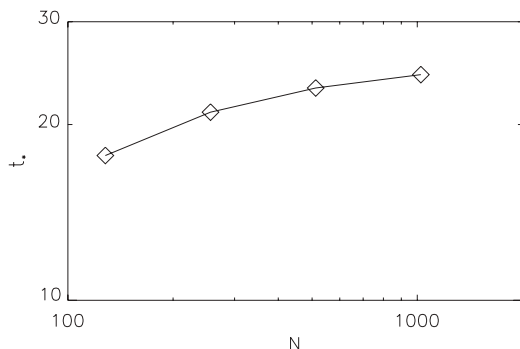


FIG. 3. Time t_* for 50% of the pseudoenstrophy to thermalize in the inviscid runs as a function of the resolution N .

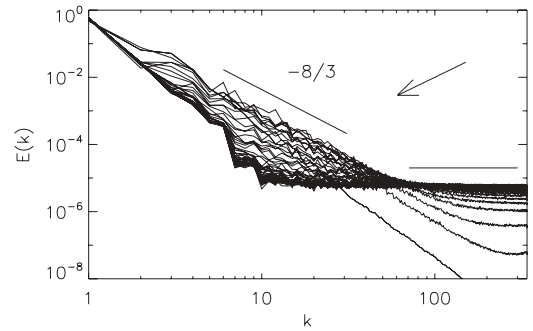


FIG. 4. Evolution of the pseudoenergy spectra for the inviscid run with $N = 1024$ from $t = 1$ to $t = 205$ with time increments $\Delta t = 4$. A $k^{-8/3}$ power law followed by an equilibrium subrange is observed for early times. As time evolves, more modes approach the equilibrium spectrum. The Gibbs ensemble prediction is indicated as a reference by the horizontal line. The arrow indicates the direction in which the spectrum evolves in time.

In the following we define the thermalized pseudoenergy and pseudoenstrophy, respectively, as the sum of the pseudoenergy and pseudoenstrophy contained in all modes with $k \geq k_{th}$,

$$E_{th} = \sum_{k=k_{th}}^{k_{max}} E(k), \quad G_{th} = \sum_{k=k_{th}}^{k_{max}} G(k). \quad (28)$$

In a similar way, we define the nonthermalized pseudoenergy and pseudoenstrophy as the difference between the total amount of these quantities (which is constant in time) and their thermalized values,

$$E_{nth} = E - E_{th}, \quad G_{nth} = G - G_{th}. \quad (29)$$

The time evolution of E_{th} , E_{nth} , G_{th} , and G_{nth} normalized, respectively, by E and G is shown in Fig. 6. E_{th} and G_{th} grow monotonically at early times, converging to an almost constant value for long times. This is consistent with Figs. 4 and 5, where more and more modes approach the statistical equilibrium solution as time evolves. This is also illustrated by the evolution of k_{th} in Fig. 7. As most of the

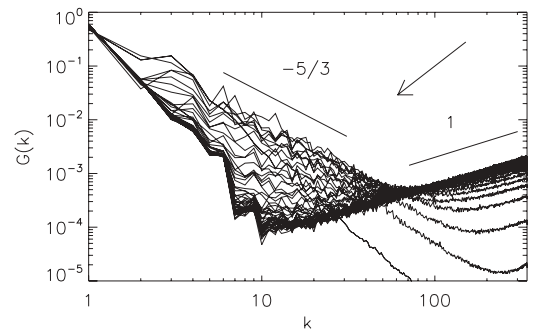


FIG. 5. Evolution of the pseudoenstrophy spectra for the inviscid run with $N = 1024$ from $t = 1$ to $t = 205$ with time increments $\Delta t = 4$. A $k^{-5/3}$ power law followed by a thermalized subrange is observed for early times. As time evolves, more modes achieve thermalization. The Gibbs ensemble prediction is indicated as a reference by the $\sim k$ line. The arrow indicates the direction in which the spectrum evolves in time.

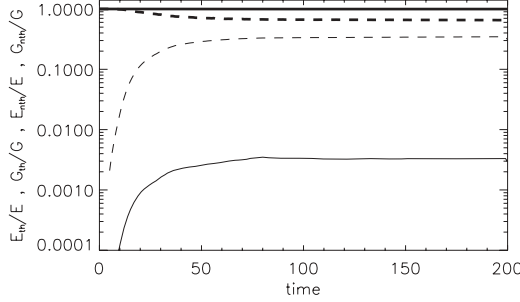


FIG. 6. Time evolution of the thermalized pseudoenergy (thin solid) and pseudoenstrophy (thin dashed line) normalized by the total pseudoenergy and pseudoenstrophy for the 1024^2 run. Both magnitudes grow monotonically towards their equilibrium asymptotic value. Nonthermalized pseudoenergy (thick solid) and pseudoenstrophy (thick dashed) normalized, respectively, by total pseudoenergy and pseudoenstrophy are also shown.

pseudoenergy condenses at $k = 1$, E_{th} remains a small fraction of the total pseudoenergy while E_{nth} (which in this case represents the condensed pseudoenergy) stays almost constant. On the other hand, G_{th} grows to a larger fraction of the total pseudoenstrophy as the $\sim k$ thermalized spectrum for G at large wave numbers (see Fig. 5) holds a significant fraction of the pseudoenstrophy in the system.

As shown in Ref. [16] for the truncated Euler equations, although the truncated system is inviscid, the transfer of pseudoenstrophy towards thermalized modes before the equilibrium is reached (resulting in the growth of E_{th} and G_{th} in time) can be interpreted as a viscouslike transient in which the thermalized modes give rise to an effective viscosity acting on the nonthermalized range. This effective viscosity is responsible for the development of turbulent inertial subranges. In the next subsection we analyze in more detail this transient, comparing the inviscid system with viscous solutions.

B. Inviscid vs dissipative systems

We focus now on the period of time when E_{th} and G_{th} are time dependent, and the flux of pseudoenstrophy towards thermalized modes can be interpreted as an out-

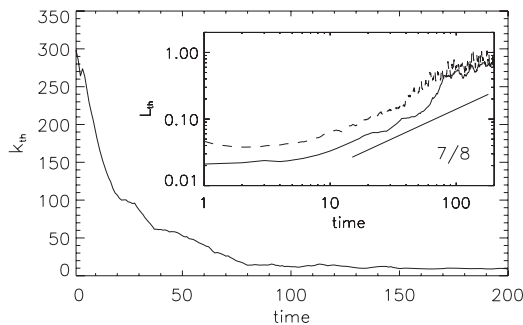


FIG. 7. Time evolution of k_{th} for the inviscid run with $N = 1024$. As time evolves, more modes reach thermalization, but k_{th} does not converge to zero as condensation of pseudoenergy takes place at the gravest modes. (Inset) Time evolution of $L_{th} = 2\pi/k_{th}$ for the inviscid runs with $N = 1024$ (solid) and with $N = 512$ (dashed) with a $\sim t^{7/8}$ slope shown as a reference.

of-equilibrium turbulent solution for $k < k_{th}$, with effective viscosity associated with the thermalized modes with $k > k_{th}$. We show that during this period, the ideal truncated model can give valuable information on the behavior of a similar but dissipative system (by similar, we mean a viscous system subject to the same initial conditions). With this aim, we compare ideal and dissipative spectra and decays for this particular period of time.

To consider dissipative SQG flows, we must solve Eq. (5) with the addition of a dissipative term,

$$\frac{\partial \hat{\psi}}{\partial t} = \frac{1}{|\mathbf{k}|} (\widehat{\partial_x q \partial_y \psi} - \widehat{\partial_x \psi \partial_y q}) - \nu |\mathbf{k}|^2 \hat{\psi}. \quad (30)$$

We solve this equation in the same way as in the ideal case, with a pseudospectral method with the 2/3 rule for dealiasing, and with second-order Runge-Kutta to evolve in time.

Equation (30) in terms of the scalar q in real space reads

$$\frac{\partial q}{\partial t} = -\mathbf{u} \cdot \nabla q + \nu \Delta q. \quad (31)$$

Multiplying the equation by q the following conservation law follows:

$$\frac{1}{2} \frac{\partial q^2}{\partial t} = -\frac{1}{2} \nabla \cdot (q^2 \mathbf{u}) + \nu q \Delta q. \quad (32)$$

Integrating over the entire domain, the first term on the right-hand side cancels and Eq. (32) in Fourier space results

$$\frac{dG}{dt} = \frac{d}{dt} \int_0^\infty G(k) dk = -2\nu \int_0^\infty k^2 G(k) dk = -\sigma, \quad (33)$$

with σ the pseudoenstrophy dissipation rate. Introducing a dissipation wave number k_η such that all dissipation is concentrated in Fourier space between $k = 1$ and $k = k_\eta$, in the turbulent steady state we can approximate

$$\sigma \approx 2\nu \int_1^{k_\eta} k^2 G(k) dk. \quad (34)$$

From Ref. [25], $G(k) \sim \sigma^{2/3} k^{-5/3}$, and replacing in Eq. (34) we finally get

$$k_\eta \sim \left(\frac{\sigma}{\nu^3} \right)^{1/4}. \quad (35)$$

This relation is important to fix the resolution in viscous simulations so that all relevant scales in the flow are well resolved. In practice, we want the dissipation wave number to be smaller than the maximum resolved wave number k_{max} , or in other words, we ask for the condition,

$$\left[\sum_1^{k_{max}} \frac{k^2 G(k)}{\nu^2} \right]^{1/4} \leq \frac{N}{3} \quad (36)$$

to be fulfilled at all times.

In Fig. 8 we show the pseudoenergy spectra at different times for the 1024^2 ideal truncated run, and for a 1024^2 well-resolved viscous run with $\nu = 4 \times 10^{-4}$. At early times, the pseudoenstrophy contained at large scales is transferred to smaller scales, and is eventually affected by thermalization or by viscous dissipation in the ideal or viscous case, respectively. These effects are different, as thermalization is a time-dependent problem which results in a time-dependent effective

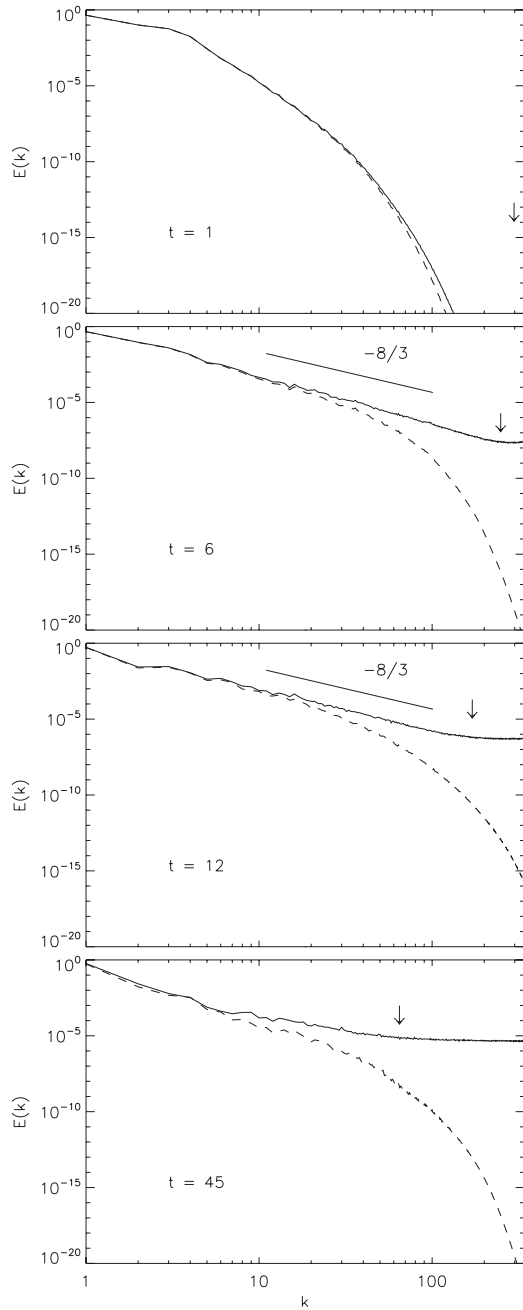


FIG. 8. Pseudoenergy spectra at different times for 1024^3 inviscid (solid) and viscous (dashed) runs. Both runs develop a power law compatible with $\sim k^{-8/3}$ (indicated as a reference by the straight line). Later on, the spectra differ at intermediate and large wave numbers, with the gravest modes still showing similar amplitudes. The arrows indicate the values of k_{th} at each time.

viscosity (see, e.g., [16,18]), while viscosity in the dissipative run is fixed. However, the large scales of both systems are similar at low wave numbers, with both systems developing a $\sim k^{-8/3}$ power law in the pseudoenergy in accordance with the theoretical results (although this subrange is wider at early times in the inviscid truncated run). This power law is lost at later times in the inviscid run, although the amplitude of the gravest modes still shows agreement with the viscous run.

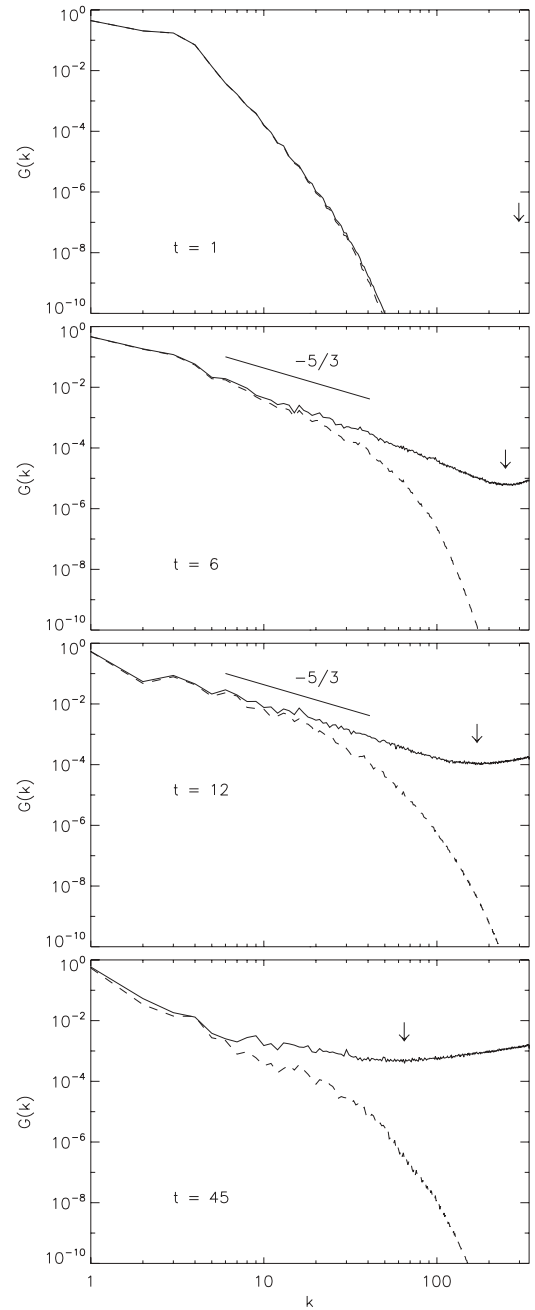


FIG. 9. Pseudoenergy spectra at different times for the same 1024^3 inviscid (solid) and viscous (dashed) runs shown in Fig. 8. A $\sim k^{-5/3}$ slope is shown as a reference. The arrows indicate the values of k_{th} at each time.

A similar behavior is observed in the time evolution of the pseudoenergy spectrum (see Fig. 9).

The similitude in the evolution of the large-scale spectra in viscous and inviscid runs makes it plausible to compare the decay of quadratic quantities in the viscous simulations, say $G(t)$, with the evolution of the associated nonthermalized quantity $G_{nth}(t)$ in inviscid truncated runs. In freely decaying turbulent flows, quadratic quantities often develop a self-similar decay law in time, once turbulence develops and dissipation sets in. The power law obeyed during this decay [in this example, say, $G(t) \sim t^{-\Lambda}$] often requires large resolution as viscous effects

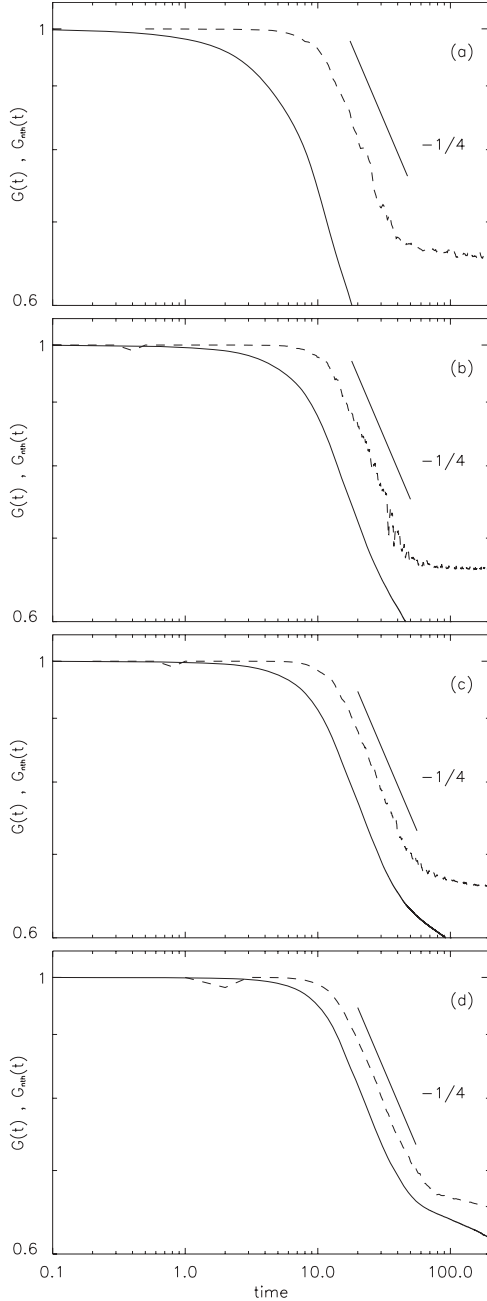


FIG. 10. Decay of pseudoenstrophy $G(t)$ in viscous runs (solid line) and time evolution of $G_{nth}(t) = G - G_{th}(t)$ in ideal truncated runs (dashed lines) at increasing resolution: (a) $N = 128$, $\nu = 2 \times 10^{-3}$, (b) $N = 256$, $\nu = 5 \times 10^{-4}$, (c) $N = 512$, $\nu = 2.5 \times 10^{-4}$, and (d) $N = 1024$, $\nu = 9 \times 10^{-5}$. The viscous $G(t)$ approaches $G_{nth}(t)$ as the Reynolds number is increased. A $\sim t^{-1/4}$ decay is indicated as a reference. The dissipation wave numbers for each viscous run are as follows: $k_\eta = 36$ for $N = 128$, $k_\eta = 84$ for $N = 256$, $k_\eta = 150$ for $N = 512$, and $k_\eta = 318$ for $N = 1024$, while the maximum resolved wave number is $k_{max} = N/3$.

tend to affect the decay, making determination of the decay rate from the simulations difficult.

In Fig. 10, we compare the decay of the pseudoenstrophy in several dissipative runs with the evolution of $G_{nth}(t)$ in inviscid runs at different grid sizes. In all viscous cases, the pseudoenstrophy is quasiconserved at early times, and then a

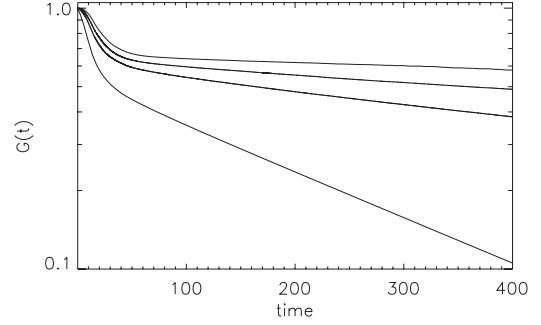


FIG. 11. Decay of pseudoenstrophy $G(t)$ for viscous runs $N = 1024$, $N = 512$, $N = 256$, $N = 128$ from top to bottom in semilog scale. Note the exponential decay after $t \approx 80$.

self-similar decay develops following a power law compatible (at the largest Reynolds numbers and spatial resolution) with $G(t) \sim t^{-1/4}$. It is worth noting that such a decay is also compatible with the strict mathematical bounds for the decay of pseudoenstrophy derived in Refs. [38,40]. The decay is followed by a saturation and a viscous exponential decay of the pseudoenstrophy that remains in the system (see Fig. 11).

The nonthermalized $G_{nth}(t)$ in all the inviscid runs shows the same evolution, which except for a small delay in the time when the quasiconservation is broken (see Fig. 12 and inset), is independent of the spatial resolution considered. Remarkably, the evolution of $G(t)$ seems to approach, as the Reynolds number is increased, the behavior of $G_{nth}(t)$, to the point that the decay $\sim t^{-1/4}$ can be identified in $G_{nth}(t)$ at much lower resolution (e.g., grid sizes of 128^2 or 256^2 grid points) than in the viscous run.

In this light, the decay of viscous SQG can be understood as follows. At early times, $G(t)$ remains approximately constant as the inertial range spectrum develops. As the smallest scales have not been excited yet, dissipative effects are negligible. Once turbulence develops, the decay law $G(t) \sim t^{-1/4}$ is observed. The decay rate in this stage is dominated by the turbulent cascade of the pseudoenstrophy towards smaller scales, and the time evolution is given by the balance equation $dG/dt = -\sigma$ where the flux of pseudoenstrophy σ is controlled by the nonlinear term in the equation, and independent

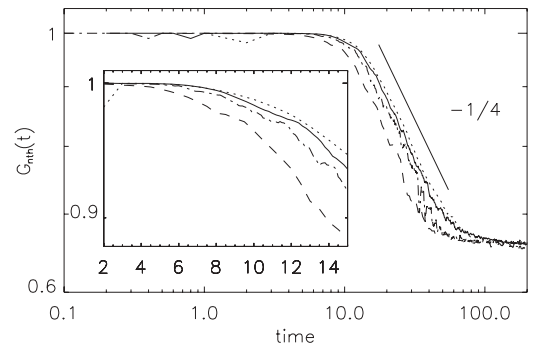


FIG. 12. Evolution of G_{nth} for different grid sizes: $N = 128$ (dashed), 256 (dash-dotted), 512 (dash-triple-dotted), and 1024 (dotted). There is small delay in the time when the decay begins as the grid size (or equivalently, k_{max}) is increased, shown in more detail in the inset. Except for this delay, all runs show the same decay, with a $\sim t^{-1/4}$ decay shown as a reference.

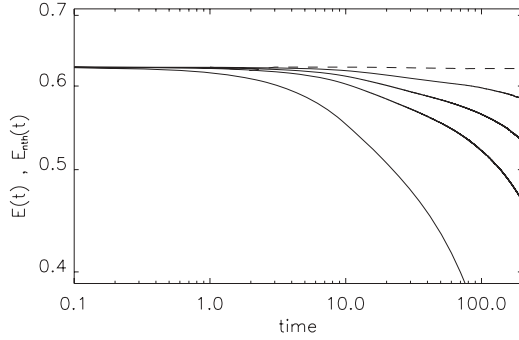


FIG. 13. Comparison between E_{nth} in an $N = 1024$ truncated inviscid simulation (dashed line) and $E(t)$ for viscous simulations with $N = 128$ ($\nu = 2 \times 10^{-3}$), 256 ($\nu = 5 \times 10^{-4}$), 512 ($\nu = 2.5 \times 10^{-4}$), and 1024 ($\nu = 9 \times 10^{-5}$) (bottom to top).

of the value of the viscosity ν as long as the Reynolds number is large enough. As a result, the truncated inviscid run, although it has a different effective viscosity, shows the same decay. Later, all pseudoenergy that remains in the system is associated with the condensation of pseudoenergy at $k = 1$, and this remaining pseudoenergy (as well as the pseudoenergy) can only decay exponentially in the viscous run (Fig. 11), while it remains constant in the inviscid run (Fig. 12).

Figure 13 compares the nonthermalized fraction of the pseudoenergy $E_{nth}(t) = E - E_{th}(t)$ in the $N = 1024$ simulation with the decay of $E(t)$ in the viscous simulations with $N = 128, 256, 512$, and 1024. In the inviscid case, as most of the pseudoenergy condenses, there is no significant change in E_{nth} with time. The viscous runs approach this behavior as the viscosity is decreased, in agreement with Batchelor-Kraichnan-Leith phenomenology for systems with condensation of one invariant at large scales (see, e.g., similar arguments for the decay of the enstrophy while the energy remains approximately constant in 2D Navier-Stokes [50]). It is worth noting that a slowdown in the decay of the pseudoenergy as the viscosity was decreased was already observed in Ref. [42].

So far, random initial conditions were used in all runs. To analyze sensitivity of the decay to other initial conditions, we briefly discuss results for three initial conditions often used in studies of singularities in the QG equations [37,42,51]:

$$\text{(I)} \quad q(t=0) = \sin(x)\sin(y) + \cos(y), \quad (37)$$

$$\text{(II)} \quad q(t=0) = -(\cos(2x)\cos(y) + \sin(x)\sin(y)), \quad (38)$$

$$\text{(III)} \quad q(t=0) = \cos(2x)\cos(y) + \sin(x)\sin(y) + \cos(2x)\sin(3y). \quad (39)$$

Initial condition **I** was used in Ref. [42] and has a hyperbolic saddle in the isolevels of the scalar, as discussed in the introduction. Initial conditions **I**, **II**, and **III** were also used in Ref. [37] to study numerically the formation of sharp fronts in the scalar field.

Conditions **II** and **III** lead to the same decay of the pseudoenergy $\sim t^{-1/4}$ as observed in the previous simulations (see Fig. 14). However, initial condition **I** results in a much slower decay (not shown), and up to the time we integrated the equations we were unable to identify any power law.

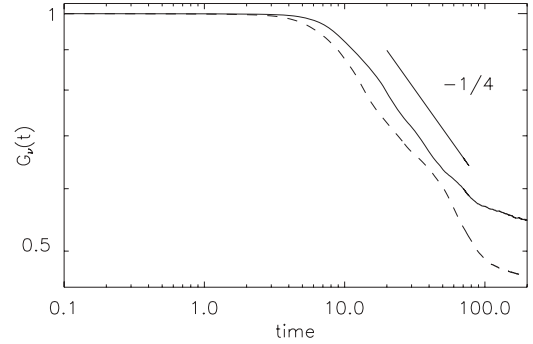


FIG. 14. Evolution of the pseudoenergy for simulations with initial conditions **II** and **III**, $N = 1024$ and $\nu = 9 \times 10^{-5}$. Both runs show a decay compatible with $G(t) \sim t^{-1/4}$.

Further analysis showed that the flow resulting from this initial condition, which initially activates only a few modes in Fourier space, develops a much steeper pseudoenergy and pseudoenergy spectra. As discussed above, a fully developed turbulent spectrum is needed to observe the self-similar decay in the enstrophy. We note that at intermediate times ($t \approx 10$), the pseudoenergy spectrum for this initial condition is $G(k) \sim k^{-2}$, the same as reported in Ref. [42]. As a result, we conclude that the difference between the inviscid spectra in Ref. [42] and the viscous cascade spectra $k^{-5/3}$ is due to the particular choice of the initial condition.

As previously mentioned, the $G(t) \sim t^{-1/4}$ decay observed in the other simulations is consistent with the upper limit of strict mathematical bounds derived for the decay of pseudoenergy (see, e.g., [38,40]). From the physical point of view, it is interesting that such a decay law can be related with the decay followed by other systems that develop condensates in the inviscid truncated case, and large-scale coherent structures in the viscous case (see, e.g., [52]). In 2D Navier-Stokes turbulence, the separation of scales between energy containing scales and enstrophy containing scales (as the former is concentrated at large scales while the latter is concentrated at small scales), together with assumptions of weak coupling between these scales [53,54], led to the idea that the decay of 2D Navier-Stokes turbulence can be understood as the superposition of a coherent (condensated) state, and a random phase, separated by a “fuzzy scale” following ideas developed for Bose-Einstein condensates [55]. In SQG, from the results in Sec. II, we can consider a pseudoenergy-containing scale associated with the condensation of pseudoenergy at low wave numbers, which contains almost all of the system pseudoenergy, and a pseudoenergy-containing scale concentrating most of the pseudoenergy. In the inviscid truncated case, we can easily identify the fuzzy scale delimiting these two phases with the thermalization length $L_{th} = 2\pi/k_{th}$. From Eq. (33), dimensional analysis leads to

$$\frac{dG}{dt} = -\sigma \sim \frac{G^{3/2}}{L}, \quad (40)$$

where L is a characteristic scale. Associating $L = L_{th}$, as most of the pseudoenergy is contained below that scale, Eq. (40) is only consistent with the observed decay $G(t) \sim t^{-1/4}$ if $L_{th}(t) \sim t^{7/8}$. The inset in Fig. 7 shows the time evolution of

L_{th} in the truncated inviscid runs with $N = 1024$ and $N = 512$ with random initial conditions, $t^{7/8}$ appears a reasonable fit; the other simulations are also consistent with this power law.

IV. CONCLUSIONS

We derived statistical equilibrium solutions of the truncated inviscid SQG equations, and verified their validity at late times in numerical simulations of the truncated SQG equations. Numerical spectra are in agreement with the theory at all wave numbers, although as resolution is increased it takes longer times for the system to reach equilibrium.

We also studied the evolution towards equilibrium of the ideal runs, finding that both pseudoenergy and pseudoenergy spectra develop a viscouslike inertial range with slopes $\sim k^{-5/3}$ and $\sim k^{-8/3}$, respectively, and compatible with Kolmogorov-Batchelor-Kraichnan phenomenology. Note that in previous studies of the inviscid SQG equations, a steeper power law was observed [42], but the initial conditions \mathbf{I} that were used result in steeper spectra for the pseudoenergy and pseudoenergy. As time evolves, the pseudoenergy in our runs shows a gradual thermalization of higher wave-number modes with $G(k) \sim k$, narrowing the viscouslike inertial range. The spectrum for the pseudoenergy presents a fat scaling for high wave numbers and a peak at $k = 1$, showing condensation of pseudoenergy at small wave numbers instead of thermalization.

Defining G_{th} and E_{th} , respectively, as the pseudoenergy and pseudoenergy contained in the thermalized modes, we studied the period of time during which these quantities are time dependent. Through this period, the transfer of pseudoenergy towards thermalized modes results in a viscouslike cascade with effective viscosity associated with the thermalized modes. This allowed us to compare spectra and decay in ideal runs with runs subjected to identical initial conditions but with the addition of dissipation. The large scales of both systems are similar and both systems develop a $\sim k^{-8/3}$ power law for the pseudoenergy in accordance with the theoretical results. At later times, the power law is lost due to thermalization in the inviscid runs and dissipation in the viscous runs.

We compared the free decay of $G(t)$ with the time evolution of the nonthermalized $G_{\text{nth}}(t)$ in inviscid truncated runs for

different grid sizes. Following an initial period of time in which the pseudoenergy is quasiconserved, viscous cases develop a power-law decay compatible with $G(t) \sim t^{-1/4}$ for the largest Reynolds numbers and spatial resolutions considered. Later in time, the decay becomes shallower and an exponential viscous decay of the remaining pseudoenergy follows. The power-law decay is in agreement with strict mathematical bounds for the decay of the pseudoenergy [38,40], and seems to be robust for initial conditions in which most of the pseudoenergy is held at the lowest modes. From the point of view of the statistical equilibrium solutions, the decay law can be understood as the result of two decaying phases weakly interacting and separated by a fuzzy scale: a coherent (condensated) state that contains most of the pseudoenergy, and a random phase that contains most of the pseudoenergy.

With the exception of a small delay in the time when the quasiconservation is broken, all the inviscid runs show the same evolution for the nonthermalized $G_{\text{nth}}(t)$ independently of the spatial resolution considered. The evolution of $G(t)$ approaches that of G_{nth} as the Reynolds number is increased. Remarkably, inviscid systems as small as 128^2 already give information about the free decay law expected for high Reynolds viscous systems.

This good agreement between the evolution of the nonthermalized components of the pseudoenergy and the pseudoenergy in truncated inviscid runs at low resolution, and of the decay of pseudoenergy and pseudoenergy in viscous runs at large resolution, further indicate a new application of inviscid simulations: that of estimating the decay law followed by the viscous system at very large Reynolds numbers. In this light, the decay of pseudoenergy in SQG turbulence in the limit of very large Reynolds numbers would be compatible with $G(t) \sim t^{-1/4}$ when all initial perturbations are at the gravest modes in the system. It is unclear for the moment whether the evolution of nonthermalized quantities in other inviscid truncated systems can be also used as proxies of decay. This problem is left for future work.

ACKNOWLEDGMENTS

The authors acknowledge support from Agencia Nacional de Promoción Científica y Tecnológica PICT Grant No. 2007-02211, Universidad de Buenos Aires UBACyT Grant No. 20020090200692, and Consejo Nacional de Investigaciones Científicas y Técnicas PIP Grant No. 11220090100825.

-
- [1] L. Onsager, *Nuovo Cimento Suppl.* **6**, 279 (1949).
 - [2] T. D. Lee, *Quart. Appl. Math.* **10**, 69 (1952).
 - [3] R. H. Kraichnan, *Phys. Fluids* **10**, 1417 (1967).
 - [4] D. G. Fox and S. A. Orszag, *Phys. Fluids* **16**, 169 (1973).
 - [5] R. H. Kraichnan, *J. Fluid Mech.* **67**, 155 (1975).
 - [6] R. H. Kraichnan and D. Montgomery, *Rep. Prog. Phys.* **43**, 547 (1980).
 - [7] R. H. Kraichnan, *J. Fluid Mech.* **59**, 745 (1973).
 - [8] T. Stribling and W. H. Matthaeus, *Phys. Fluids B* **2**, 1979 (1990).
 - [9] S. Servidio, W. H. Matthaeus, and V. Carbone, *Phys. Plasmas* **15**, 042314 (2008).
 - [10] M. L. Waite and P. Bartello, *J. Fluid Mech.* **517**, 281 (2004).
 - [11] L. Bourouiba, *Phys. Fluids* **20**, 075112 (2008).
 - [12] P. D. Mininni, P. Dmitruk, W. H. Matthaeus, and A. Pouquet, *Phys. Rev. E* **83**, 016309 (2011).
 - [13] R. Salmon, G. Holloway, and M. C. Hendershott, *J. Fluid Mech.* **75**, 691 (1976).
 - [14] U. Frisch, A. Pouquet, J. L  orat, and A. Mazure, *J. Fluid Mech.* **68**, 769 (1975).

- [15] C. Cichowlas, P. Bonaiti, F. Debbasch, and M. Brachet, *Phys. Rev. Lett.* **95**, 264502 (2005).
- [16] G. Krstulovic and M. E. Brachet, *Physica D* **237**, 2015 (2008).
- [17] U. Frisch, S. Kurien, R. Pandit, W. Pauls, S. S. Ray, A. Wirth, and J.-Z. Zhu, *Phys. Rev. Lett.* **101**, 144501 (2008).
- [18] G. Krstulovic, P. D. Mininni, M. E. Brachet, and A. Pouquet, *Phys. Rev. E* **79**, 056304 (2009).
- [19] G. Krstulovic, M. E. Brachet, and A. Pouquet, *Phys. Rev. E* **84**, 016410 (2011).
- [20] G. Krstulovic and M. Brachet, *Phys. Rev. Lett.* **106**, 115303 (2011).
- [21] A. J. Majda and X. Wang, *Nonlinear Dynamics and Statistical Theories for Basic Geophysical Flow* (Cambridge University Press, Cambridge, 2006).
- [22] J. G. Charney, *Geophys. Publ.* **17**, 3 (1948).
- [23] J. G. Charney, *J. Atmos. Sci.* **28**, 1087 (1971).
- [24] J. Pedlosky, *Geophysical Fluid Dynamics*, 2nd ed. (Springer, New York, 1987).
- [25] R. T. Pierrehumbert, I. M. Held, and K. L. Swanson, *Chaos Solitons Fractals* **4**, 1111 (1994).
- [26] I. M. Held, R. T. Pierrehumbert, S. T. Garner, and K. L. Swanson, *J. Fluid Mech.* **282**, 1 (1995).
- [27] C. V. Tran, *Physica D* **191**, 137 (2004).
- [28] C. V. Tran and J. C. Bowman, *J. Fluid Mech.* **526**, 349 (2005).
- [29] C. V. Tran and D. G. Dritschel, *Phys. Fluids* **18**, 121703 (2006).
- [30] C. V. Tran, *Physica D* **213**, 76 (2006).
- [31] M. Juckes, *J. Atmos. Sci.* **51**, 2756 (1994).
- [32] G. Hakim, C. Snyder, and D. Muraki, *J. Atmos. Sci.* **59**, 2405 (2002).
- [33] R. Tulloch and K. S. Smith, *Proc. Natl. Acad. Sci. USA* **103**, 14690 (2006).
- [34] J. Isern-Fontanet, B. Chapron, G. Lapeyre, and P. Klein, *Geophys. Res. Lett.* **33**, L24608 (2006).
- [35] G. Lapeyre and P. Klein, *J. Phys. Oceanogr.* **36**, 165 (2006).
- [36] J. H. LaCasce and A. Mahadevan, *J. Mar. Res.* **27**, 695 (2006).
- [37] P. Constantin, A. J. Majda, and E. Tabak, *Nonlinearity* **7**, 1495 (1994).
- [38] P. Constantin and J. Wu, *Siam J. Math. Anal.* **30**, 937 (1999).
- [39] P. Constantin, D. Córdoba, and J. Wu, *Indiana Univ. Math. J.* **50**, 97 (2001).
- [40] A. Córdoba and D. Córdoba, *Commun. Math. Phys.* **249**, 511 (2004).
- [41] D. Córdoba, *Ann. Math.* **148**, 1135 (1998).
- [42] K. Ohkitani and M. Yamada, *Phys. Fluids* **9**, 876 (1997).
- [43] D. Bernard, G. Boffetta, A. Celani, and G. Falkovich, *Phys. Rev. Lett.* **98**, 024501 (2007).
- [44] K. S. Smith, G. Boccaletti, C. Chenning, I. Marinov, C. Y. Tam, I. M. Held, and G. K. Vallis, *J. Fluid Mech.* **469**, 13 (2002).
- [45] W. Blumen, *J. Atmos. Sci.* **35**, 774 (1978).
- [46] V. D. Larichev and J. C. McWilliams, *Phys. Fluids A* **3**, 938 (1991).
- [47] D. O. Gomez, P. D. Mininni, and P. Dmitruk, *Phys. Scr.* **T116**, 123 (2005).
- [48] P. D. Mininni, D. Rosemberg, R. Reddy, and A. Pouquet, *Parallel Computing* **37**, 316 (2011).
- [49] C. Canuto, M. Y. Hussaini, A. Quarteroni, and T. A. Zang, *Spectral Methods. Fundamentals in Single Domains* (Springer, Heidelberg, 2006).
- [50] G. K. Batchelor, *Phys. Fluids* **12**, 233 (1969).
- [51] K. Ohkitani and T. Sakajo, *Nonlinearity* **23**, 3029 (2010).
- [52] V. Yakhot, *Phys. Rev. Lett.* **93**, 014502 (2004).
- [53] J.-P. Laval, B. Dubrelle, and S. Nazarenko, *Phys. Rev. Lett.* **83**, 4061 (1999).
- [54] J.-P. Laval, B. Dubrille, and S. Nazarenko, *Physica (Amsterdam)* **142D**, 231 (2000).
- [55] N. N. Bogolubov, *Sov. Phys. JETP* **7**, 41 (1958).